

Richtmyer–Meshkov instability growth: experiment, simulation and theory

By RICHARD L. HOLMES¹, GUY DIMONTE²,
BRUCE FRYXELL³, MICHAEL L. GITTINGS^{1,4},
JOHN W. GROVE^{1,5}, MARILYN SCHNEIDER²,
DAVID H. SHARP¹, ALEXANDER L. VELIKOVICH⁶,
ROBERT P. WEAVER¹ AND QIANG ZHANG⁴

¹ Los Alamos National Laboratory, Los Alamos, NM 87545, USA

² Lawrence Livermore National Laboratory, Livermore, CA 94551, USA

³ Department of Physics and Atmospheric Science, Drexel University, Philadelphia, PA 19104,
USA and Goddard Space Flight Center, NASA, Greenbelt, MD 20771, USA

⁴ Science Applications International Corporation, San Diego, CA 92121, USA

⁵ Department of Applied Mathematics and Statistics, University at Stony Brook, Stony Brook,
NY 11794-3600, USA

⁶ Berkeley Research Associates, PO Box 852, Springfield, VA 22510-0852, USA

(Received 5 January 1998 and in revised form 4 September 1998)

Richtmyer–Meshkov instability is investigated for negative Atwood number and two-dimensional sinusoidal perturbations by comparing experiments, numerical simulations and analytic theories. The experiments were conducted on the NOVA laser with strong radiatively driven shocks with Mach numbers greater than 10. Three different hydrodynamics codes (RAGE, PROMETHEUS and FronTier) reproduce the amplitude evolution and the gross features in the experiment while the fine-scale features differ in the different numerical techniques. Linearized theories correctly calculate the growth rates at small amplitude and early time, but fail at large amplitude and late time. A nonlinear theory using asymptotic matching between the linear theory and a potential flow model shows much better agreement with the late-time and large-amplitude growth rates found in the experiments and simulations. We vary the incident shock strength and initial perturbation amplitude to study the behaviour of the simulations and theory and to study the effects of compression and nonlinearity.

1. Introduction

Richtmyer–Meshkov instability (RMI) (Meshkov 1969, 1970; Richtmyer 1960) is generated when a shock wave refracts through the interface between two materials. Perturbations on the interface grow in size and cause the materials to mix. RMI plays an important role in inertial confinement fusion (ICF), where small capsules containing a deuterium-tritium fuel are compressed by laser-generated shock waves. The goal is to achieve sufficiently high pressures and temperatures inside the compressed ICF targets to ignite the fuel. Mixing due to instabilities on the interface between the outer shell and the inner fuel inhibits the fusion reaction and can be a limiting factor in the energy produced (Emery *et al.* 1991; Ishizaki & Nishihara 1997; Lindl, McCrory & Campbell 1992; Taylor *et al.* 1997).

Even in the simplest case of a plane shock hitting a sinusoidally perturbed interface

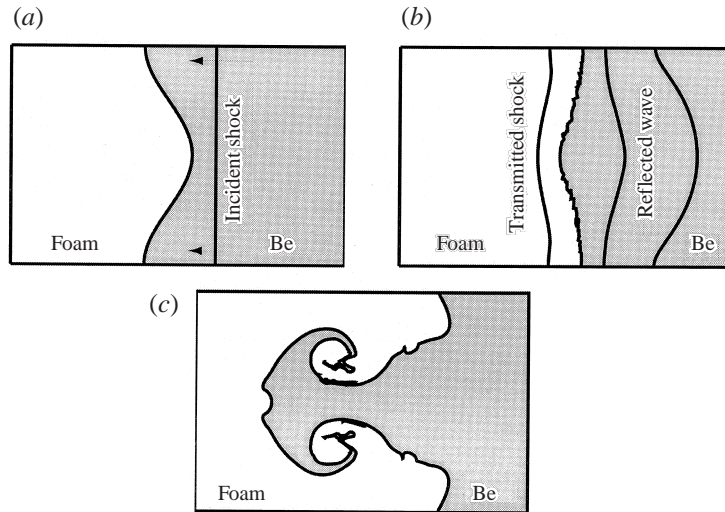


FIGURE 1. Computation of NOVA RMI experiments. (a) A shock wave moves toward the interface between beryllium (shaded) and foam (unshaded). (b) The shock wave has refracted through the interface and deposited vorticity along the interface that will drive perturbation growth. The transmitted shock and the two edges of the reflected rarefaction wave are also shown. (c) Late-time interface showing the characteristic mushroom shape. The transmitted and reflected waves have left the region shown in the figure.

(see figure 1) experiments, numerical simulations and theoretical models have given conflicting values for the growth rate of the perturbations (Benjamin 1992; Benjamin, Besnard & Haas 1993; Besnard *et al.* 1991; Cloutman & Wehner 1992; Meshkov 1970; Meyer & Blewett 1972; Richtmyer 1960). The discrepancy between experimentally measured and predicted growth rates has been attributed to strength and porosity effects of the membrane used to separate the gases in shock tube experiments (Cloutman & Wehner 1992; Meshkov 1970; Meyer & Blewett 1972) and boundary layer effects (Vetter & Sturtevant 1995). The critical importance of late-time nonlinearity in RMI, independent of the experimental issues just mentioned, was shown in Grove *et al.* (1993) and Holmes, Grove & Sharp (1995). In Holmes *et al.* (1995) simulations were performed for relevant experimental times that showed greatly improved agreement with experimental data while agreeing very well with previously published early-time results. It was also shown that the linear theory accurately predicts growth rates for very early times and small initial amplitudes. At later times the perturbation growth rate decreases significantly due to nonlinear effects and the growth rates predicted by the linear theory are too large. A theory for compressible RMI which accounts for these nonlinear effects is developed in Zhang & Sohn (1996, 1997*a, b*). The theoretical predictions are in excellent agreement with the results from numerical simulations and experimental data considered in Benjamin (1992), Grove *et al.* (1993) and Holmes *et al.* (1995).

The present study has a two-fold purpose. First, we compare growth rates from experiment, simulation and theory in the conditions relevant to ICF. Second, simulations based on different codes and different models are compared in a controlled way so that differences in the results can be understood and clarified. We find that experiments and simulations generally agree well and that in most cases the compressible nonlinear theory does a good job of predicting the time history of the perturbation growth rates.

The experiments are conducted on the Lawrence Livermore National Laboratory NOVA laser using beryllium and foam plasmas and have many features that are useful for comparison to simulation and models. These features include the lack of a membrane separating the materials and the availability of data over both early and late time scales. However, the experiments also contain effects not found in the simulations or models. In particular, radiation is not included and the simulations and the theories use perfect gas equations of state. A discussion of these issues is given in §2.1.2.

The experimental data used here are from previously published results using the Lawrence Livermore NOVA laser (Dimonte *et al.* 1996; Dimonte & Remington 1993). The numerical simulations are performed using three different codes: the front tracking code *Frontier* (Grove *et al.* 1993; Holmes *et al.* 1995), the PPM-based code *PROMETHEUS* (Fryxell, Müller & Arnett 1989), and the AMR code *RAGE* (Baltrusaitis *et al.* 1996; Gittings 1992). The theoretical predictions are taken from the impulsive model of Richtmyer (Richtmyer 1960), the linear theory of RMI for the case of a reflected rarefaction wave formulated in Yang, Zhang & Sharp (1994), a nonlinear theory for compressible fluids driven by a shock wave (Zhang & Sohn 1996) and a nonlinear theory for incompressible fluids driven by an impulsive force (Velikovich & Dimonte 1996).

In addition to the experimental conditions, we give the simulation and modelling results for a broader range of conditions, both to investigate the changes in interfacial behaviour and to illustrate the behaviour and degree of validity of the theories in different regimes.

A completely specified list of the parameters and initial conditions used in the simulations and models is provided in the appendix so that other workers can benchmark their results against those reported here.

2. Descriptions of experiments, codes and models

2.1. Experiment

2.1.1. Experimental configuration

The experiments were conducted on the NOVA laser at Lawrence Livermore National Laboratory as described in Dimonte *et al.* (1996). The shocks were generated with an indirect drive configuration by focusing the laser beams (28 kJ, 3 ns) into a radiation enclosure (hohlraum). This creates a uniform quasi-Planckian X-ray spectrum, whose equivalent radiation temperatures $T_r \sim 110$ eV (LOW drive) and $T_r \sim 140$ eV (HIGH drive) are varied by changing the hohlraum size (~ 1 mm). The drive X-rays heat a target mounted on a $740 \mu\text{m}$ diameter hole in the hohlraum wall, producing an expanding ablation plasma at the surface and a shock moving into the target. The target consists of a beryllium ablator ($\rho_{Be} = 1.7 \text{ g cm}^{-3}$, depth $\Delta z \sim 100 \mu\text{m}$ and $800 \mu\text{m}$ by $800 \mu\text{m}$ cross-section) and a low-density foam tamper ($\rho_f = 0.12 \text{ g cm}^{-3}$, $\Delta z \sim 900 \mu\text{m}$ and $800 \mu\text{m}$ by $400 \mu\text{m}$ cross-section) in planar geometry. The foam is a CHO matrix doped with Na_2WO_4 to adjust its X-ray opacity whereas the beryllium is transparent to the diagnostic X-rays. Two-dimensional sinusoidal perturbations are imposed at the interface and diagnosed with face-on and side-on radiography.

In addition to the perturbation amplitude we measure the shock and interface speeds and the foam post-shock density. The beryllium density and the X-ray preheat are calculated in one dimension with the *LASNEX* simulation code (Zimmerman & Kruer 1975) which uses the measured X-ray drive $T_r(t)$, multi-group radiation

diffusion and tabulated equations of state. The calculations reproduce the measured quantities very well (Dimonte *et al.* 1996). They also indicate that the beryllium has a density of approximately 2 g cm^{-3} after shocking and subsequent expansion by the reflected rarefaction and that the target is pre-heated to 1–2 eV (11 000–22 000 K) ahead of the shock by the high-energy X-rays, leaving both the beryllium and the foam in a plasma state.

2.1.2. Approximations for simulations and models

Radiation drive and real equations of state are complex. Since our goal is to study the basic hydrodynamics of the induced RMI the simulations and models use a pressure drive and ideal gas equations of state.

We determine values of the pressure drive and polytropic exponents γ_{Be} (beryllium) and γ_f (foam) as follows. The drive pressures are obtained from the peak ablation pressures computed by LASNEX and are 30 and 15 Mbar for the HIGH and LOW drives, respectively. The LASNEX simulations also indicate that the main effect of the X-ray preheat is to heat the upstream materials to approximately 1–2 eV. Little motion occurs before the shock reaches the interfaces and therefore the initial densities are nearly preserved. Under these conditions the initial pressure ahead of the incident shock is 0.1 Mbar. The effective heat capacity ratios ($\gamma = 1.8$ for beryllium and 1.45 for foam) are obtained by solving the Riemann problem for this two-fluid configuration to match observed shock-induced velocities and compressions. These values give a sound speed of $3.254 \mu\text{m ns}^{-1}$ in the unshocked beryllium that is used for calculating the Mach numbers.

By ignoring radiation and real equation-of-state effects there is the possibility that the conditions used for the simulations and models are different in significant ways from the conditions in the experiments. In a radiatively driven system such as was used in the experiments the fluid state behind the driving shock is typically not constant. In addition, if the X-ray preheat preferentially heats one material over another or results in excessively high temperatures then movement of the interface before shocking or non-uniformity in the fluid states may result. The LASNEX simulations in Dimonte *et al.* (1996) show, however, that this is not the case. Differences in the equations of state would lead to different shocked material densities and affect shock and interface speeds. Referring to table 1 we see that the shocked-foam density, ρ_f^* , and the incident shock speed are well approximated by the ideal gas model but that the interface and transmitted shock velocities are 15–20% too small. This is comparable to the experimental error in the shock-induced velocities and perturbation amplitude. Using the Impulsive Model (§2.3.1) to get a crude estimate of the effect of the speed differences we find that the relative change in the growth rate should be nearly the same as the relative change in interface velocity. We conclude, then, that 15–20% differences in amplitudes and growth rates between calculations and measurements should be regarded as due to theoretical simplifications and experimental uncertainties.

2.2. Numerical methods

2.2.1. FronTier

FronTier is a front tracking code (Chern *et al.* 1986; Grove 1987) and is designed to accurately compute solutions to problems with well-defined features, such as material interfaces and shock waves. It eliminates smearing of these waves by keeping true discontinuities at the tracked fronts and provides sub-grid resolution of wave interactions, such as shock–interface refractions. FronTier has been used with great

Qty	Drive	NOVA	Model	LASNEX
s_i	High	50	50	47
s_t		90	74	87
u_c		71	59	67
ρ_{Be}^*		—	2.3	2.2
ρ_f^*		0.6	0.6	0.6
s_i	Low	30	35	33
s_t		49	53	46
u_c		35	42	36
ρ_{Be}^*		—	2.3	2.2
ρ_f^*		0.5	0.55	0.6

TABLE 1. Experimentally measured hydrodynamic values for high and low drive experiments along with those given by the γ -law gas approximation and a one-dimensional LASNEX calculation. Initial densities of beryllium and foam are 1.7 and 0.12 g cm^{-3} . The model uses a drive pressure of 30 and 15 Mbar for high and low drive cases, a pressure of 0.1 Mbar ahead of the incident shock, and γ of 1.8 and 1.45 for beryllium and foam. All velocities are measured in $\mu\text{m ns}^{-1}$ where s_i and s_t are the incident and transmitted shock velocities, respectively, and u_c is the shocked contact velocity. ρ_{Be}^* and ρ_f^* are shocked densities in beryllium and foam in g cm^{-3} .

success in the computation of unstable interface problems in gas dynamics (Glimm *et al.* 1990; Grove *et al.* 1993; Holmes *et al.* 1995) and porous media flows (Glimm, Lindquist & Zhang 1991).

The flow in a Frontier simulation is represented by a composite grid consisting of a rectangular finite difference lattice of cell-averaged states together with lower-dimensional dynamic grids that follow the selected fronts. In two dimensions these moving grids are represented by piecewise linear curves. At each point connecting the linear elements two states are assigned corresponding to the limiting states at that point from each side of the curve. By assigning two states at each point it is possible to represent jumps in states across that wave.

Points on the tracked fronts are propagated in an operator split fashion, with a movement and state update in the direction normal to the front followed by a finite difference update in the tangential direction. The tracked fronts serve as internal boundaries for the update of lattice states through a second-order Godunov method. Care is taken not to take finite differences across waves, thus eliminating the numerical diffusion that results from using finite difference schemes at discontinuities.

If two curves cross in the course of a time step, different algorithms are invoked which resolve the wave interactions. For example, in the case of shock refraction through a material interface the incident shock crosses the material interface during the update of the front positions. The code detects this and at the intersection points creates new curves to follow the transmitted shock and reflected rarefaction wave.

2.2.2. PROMETHEUS

The PROMETHEUS code (Fryxell *et al.* 1989) solves Euler's equations on a uniform rectangular grid using the piecewise-parabolic method (PPM) (Colella & Woodward 1984; Woodward & Colella 1984). PPM belongs to the family of high-order Godunov methods, and is designed to provide an accurate treatment of discontinuities. Although the code is formally second-order accurate, the most critical steps in the method are performed to a higher order of accuracy. The method can accurately follow shocks which are one to two zones wide without introducing significant post-

shock oscillations and a contact steepening algorithm is used to reduce the diffusive spread of contact discontinuities and maintain them with a width of approximately two zones. Multiple fluids are treated by solving a separate advection equation for each material, although no fluid interfaces are explicitly tracked. PROMETHEUS has been used for astrophysical computations of a wide range of problems including instabilities in supernova explosions (Muller, Fryxell & Arnett 1991), the explosion mechanism in Type II supernovae (Burrows, Hayes & Fryxell 1995), and non-spherical accretion flows (Fryxell & Taam 1988).

2.2.3. RAGE

RAGE (Radiation Adaptive Grid Eulerian, Gittings 1992) is a multi-dimensional Eulerian radiation-hydrodynamics code developed by Los Alamos National Laboratory and Science Applications International (SAIC). RAGE features a continuous (in time and space) adaptive mesh refinement (CAMR) algorithm for following important waves, especially shocks and contact discontinuities, with a very fine grid while using a coarse grid in smooth flow regions. This allows the code to devote the bulk of the computing resources to those areas where they are needed most. Two of the key features of the adaption algorithm are the ability to subdivide or combine cells on each time-step cycle and the restriction that any two neighbouring cells differ by at most one level of refinement (a factor of two in linear dimension).

RAGE uses a second-order Godunov-type scheme similar to the Eulerian MUSCL scheme of Colella (Colella 1985). Multiple materials are handled through a separate advection step for each material (as in PROMETHEUS) and, while there is no explicit interface tracking or reconstruction algorithm, diffusion is limited at the interface by the use of the finest cells in the AMR grid. Mixed cells are assumed to be in pressure, temperature and velocity equilibrium.

RAGE has been extensively validated against a wide variety of both analytic test problems and detailed experiments. A standard set of analytic hydrodynamic test problems, which RAGE has successfully calculated, includes shock tubes with various shock strengths, self-similar blast waves and compression problems, e.g. the ‘Noh’ problems (Noh 1983). Validation against laboratory experiments include ablation-driven Rayleigh–Taylor NOVA laser experiments (G. Schappert & D. Hollowell 1996, personal communication) and Los Alamos shock tube experiments (Baltrusaitis *et al.* 1996).

2.3. Models

We also compare the results of linear and nonlinear models of Richtmyer–Meshkov instability.

2.3.1. Linear models

Linear models for RMI arise from a linearization of the Euler equations about solutions for the unperturbed flow. The linearized form of the compressible Euler equations was derived for the case of a reflected shock wave by Richtmyer (Richtmyer 1960) with the analysis extended to the case of a reflected rarefaction in Yang *et al.* (1994) and subsequently in Velikovich (1996). The linearization of the Euler equations results in a single partial differential equation in one space dimension whose solutions have been investigated numerically (Yang *et al.* 1994) and using power series in time (Velikovich 1996) with essentially identical results. Alternative methods for deriving linear growth rates are given in Samtaney & Zabusky (1994) and Wouchuk & Nishihara (1996, 1997).

The Impulsive Model, also proposed by Richtmyer (Richtmyer 1960), is a simple approximation to the compressible linear theory. In this model the effect of the shock is described by an impulse applied to the interface with the flow otherwise assumed to be incompressible. Richtmyer derived the equation for the amplitude $a(t)$ of a sinusoidal perturbation,

$$\frac{da(t)}{dt} = \dot{a}_{IM} = kA^*a_0u_c, \quad (2.1)$$

where k is the wavenumber of the perturbation ($= 2\pi/\lambda$), A^* is the post-shock Atwood ratio $(\rho_0^* - \rho_1^*)/(\rho_0^* + \rho_1^*)$ where the shock moves from fluid 1 to fluid 0, u_c is the change in interface velocity due to the action of the shock and a_0 is an appropriate initial amplitude. This equation is presumed valid for amplitudes much smaller than the wavelength ($ka(t) \ll 1$).

The derivation of (2.1) leads to an ambiguous value for the initial amplitude a_0 . In practice, a_0 is chosen to fit a certain range of data. For example, for positive A^* Richtmyer (Richtmyer 1960) chose $a_0 = a_{0+}$, the amplitude immediately after shock compression, to obtain the best agreement with his numerical data for the compressible linear theory. In Meyer & Blewett (1972) it was shown that when $A^* < 0$ better results were obtained if the initial amplitude was chosen as $a_{\pm} = \frac{1}{2}(a_{0+} + a_{0-})$, where a_{0-} is the pre-shock perturbation amplitude. It is this form which is used in this paper.

Equation (2.1) predicts a growth rate that is constant in time which is in qualitative agreement with the behaviour predicted by the linear compressible theory for intermediate and late times. At early times, when the linear theories are actually valid, the impulse model and the linear theory predict qualitatively different time dependencies for the growth rate. The regions of parameter space in which there is quantitative agreement or disagreement between the compressible linear theory and the impulse model is explored in Velikovich (1996) and Yang *et al.* (1994).

2.3.2. Nonlinear models

Both the compressible linear theory and the impulsive model lose validity once the amplitude of the perturbation at the material interface grows to a certain size. Several approaches have been taken to model the nonlinear phase of RMI growth.

Some of the approaches analyse the growth rate of the perturbation by calculating the velocities of the heavy-fluid spike and light-fluid bubble separately (Alon *et al.* 1995, 1994; Hecht, Alon & Shvarts 1994; Mikaelian 1996; Zhang 1996) using potential flow models. However, the solutions are asymptotic in time and do not apply to the early and intermediate phases of RMI and are not considered here.

Zhang & Sohn (1996, 1997*a,b*) have developed a nonlinear model for RMI in compressible fluids which is valid for any density ratio. This model is based on the idea that, for small initial perturbation amplitudes, an RM unstable system is approximately linear and compressible at early times and is nonlinear and incompressible at late times. Using Padé approximations and asymptotic matching, they derived the following expression for the perturbation growth rate:

$$\frac{da(t)}{dt} = \frac{\dot{a}_{lin}}{1 + \dot{a}_{lin}a_{0+}k^2t + \max\{0, a_{0+}^2k^2 - A^2 + \frac{1}{2}\}\dot{a}_{lin}^2k^2t^2}. \quad (2.2)$$

Here $\dot{a}_{lin} = da_{lin}(t)/dt$ is the growth rate predicted by the compressible linear theory (§2.3.1). We emphasize that no impulsive force approximation is made in deriving (2.2).

In §3 we compare the predictions of (2.2) with experimental and computational

data. We find that, with some exceptions, the predictions of the model are in good agreement with the data for the entire range of times and parameter values considered.

Velikovich & Dimonte (1996) have developed a perturbative method which systematically generates nonlinear corrections to the Impulsive Model. The method uses symbolic computation and high-order Padé approximation. The initial velocity distribution in all modes due to an impulsive force is derived and a time history of the perturbation is given for the case $A = 1$ (Velikovich & Dimonte 1996). A straightforward extension of the analysis in Velikovich & Dimonte (1996) results in the initial perturbation growth rate for the general case of $A \leq 1$. Since this is an incompressible model the initial growth rate is also the peak growth. To eighth order in the parameter $\epsilon = ka_0$ the series for the peak growth rate, \dot{a}_{peak} , is given by

$$\frac{\dot{a}_{peak}}{\dot{a}_{IM}} = 1 - \frac{1}{4}\epsilon^2 + \frac{19}{192}\epsilon^4 + \left(\frac{1}{288}A^2 - \frac{167}{3840}\right)\epsilon^6 + \left(\frac{6893}{344064} - \frac{97}{23040}A^2\right)\epsilon^8 + \dots,$$

where \dot{a}_{IM} is the growth rate given by the Impulsive Model. In actual use a Padé approximation is derived which extends the applicability of this series outside its circle of convergence $|\epsilon| < 1$. This predicted initial growth rate is compared to experimental and simulation peak growth rates in §3.1.

3. Comparison of experiment, simulation and theories

In this section we demonstrate agreement between theory, simulation and experiment for single-mode RMI in a variety of parameter regimes. We focus our analysis on the time-dependent behaviour of the amplitude of the perturbation, defined as one-half the extent of the mixing region, and of the perturbation growth rate, which is the time derivative of the amplitude.

We consider seven different initial configurations covering a substantial range of variation of initial amplitude (§3.1) and initial shock strength (§3.2). Each configuration is labelled by a pair of numbers of the form (initial perturbation amplitude)/(incident shock Mach number). For example, case 10/15.3 corresponds to an initial perturbation amplitude of $10\mu\text{m}$ and an incident shock Mach number of 15.3. In each case the perturbation wavelength is fixed at $100\mu\text{m}$. The three cases 10/15.3, 4/15.3 and 4/10.8 correspond to actual experimental conditions as described in §2.1 while the remaining four cases, 4/5.6, 4/1.33, 25/15.3 and 50/15.3, are used to illustrate the behaviour and validity of the simulations and models for a broad range of incident shock strength and initial amplitude. Discussion of the initialization and validation of the simulations is given in the Appendix.

3.1. Initial amplitude variations

The temporal evolution of our most studied case, 10/15.3, is shown in figure 2. Time is referenced to when the shock completes the interface traversal and is uncertain in the experiment by approximately 0.25 ns. We note excellent agreement among the results obtained from numerical simulations, the analytical prediction of the compressible nonlinear theory and experiment. The compressible linear theory correctly predicts the growth rate of the instability at very early times, but substantially overestimates the growth rate at intermediate and late times. The Impulsive Model gives the correct order of magnitude of the growth rate even with a five-fold compression of the foam, but it does not describe the temporal evolution. The Impulsive Model and the compressible linear theory agree at later times.

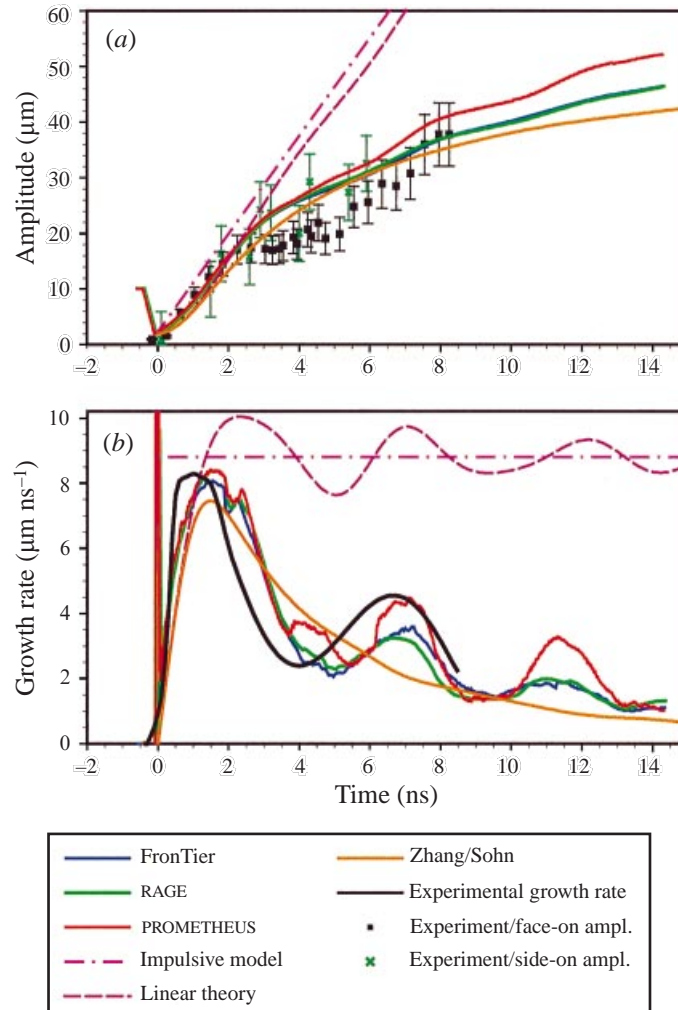


FIGURE 2. Experimental, simulation and theoretical predictions for perturbation growth for the Mach 15.3, $a_{0-} = 10\mu\text{m}$ case. (a) Amplitude vs. time. (b) Growth rate vs. time. Time $t = 0$ is defined as the time at which the refraction process is complete. Error bars indicate uncertainties in the amplitude measurements while the experimental growth rate curve in (b) is estimated to be accurate to within $1.5\mu\text{m ns}^{-1}$.

Several interesting features of the growth rate (Figure 2b) merit discussion. First, the simulations show a very large spike in the growth rate at early times. This is due to the ‘direct’ phase inversion (Yang *et al.* 1994) of the material interface during shock refraction, since the shocked interface speed, u_c , is greater than that of the incident shock speed, s_i (table 2, Appendix). This produces a fully inverted interface by the time the refraction completes. The growth rate spike occurs because, just prior to the end of the refraction, the centre part of the contact (in the geometry of Figure 1) has moved past the still unshocked outer edges of the interface. The shocked leftmost part of the interface is separating from the unshocked rightmost part at a high speed until the shock has accelerated the entire contact to approximately the same speed, causing the observed spike. Later (case 4/1.33) we show an ‘indirect’ phase inversion which occurs when $u_c < s_i$ and $da/dt < 0$.

Another interesting feature is the effect of compressibility which is manifested in two ways. First, the growth rate increases to a peak value of approximately $8.5 \mu\text{m ns}^{-1}$ which is much smaller than the uncompressed estimate, i.e. with no change in material densities or initial amplitude due to the action of the shock, $Au_c ka_{0-} \approx 27 \mu\text{m ns}^{-1}$. This effect of compressibility is significant and described by all the calculations and models. Second, compressibility is seen through the oscillations in the growth rate. The growth rate decreases dramatically near 3 ns and then oscillates with a period of approximately 5 ns. This time scale is comparable to $\lambda/c_{Be}^* = 4.8 \text{ ns}$ where $c_{Be}^* = 20.7 \mu\text{m ns}^{-1}$ is the sound speed in the shocked beryllium adjacent to the interface. This suggests that the oscillations are related to shock reverberations in the upstream beryllium generated by the curved rarefaction wave (Grove *et al.* 1993; Holmes *et al.* 1995) which is confirmed by looking at the interface velocities at the bubble and spike separately—the oscillations appear in the bubble velocity but not the spike velocity. The decay and the oscillations in the growth rate are well described by the simulations and the experiments, although it should be noted that the experimental growth rate measurement has a large uncertainty of $\pm 1.5 \mu\text{m ns}^{-1}$ since it is obtained by differentiating a sixth-order polynomial fit to the measured amplitude.

We note that after 4 ns the lateral expansion of the experimental target has increased the perturbation wavelengths by approximately 15%. This may contribute to the smaller amplitudes seen in the experiments compared to the simulations at these times.

Finally, we observe that (2.2) gives an excellent prediction for decay of the growth rate with time, within the scatter in the simulations and experiment. Because (2.2) is based on the idea that the flow is essentially incompressible at late times, the compressible effects exhibited as oscillations in the simulation and linear theory growth rate curves are much smaller or missing in the nonlinear theory. Nevertheless, the amplitude determined by integrating (2.2) in time is in good agreement with the numerical results and experimental data.

Colour images of the density from the simulations are compared with experimental side-on radiographs in figure 3. Due to the limited experimental resolution (approximately $10 \mu\text{m}$) only the large-scale features are measured and they are well described by all three simulations. The experimental interface profiles (in white) are obtained from intensity contours of the radiographs. The shock is approximately 20% faster in the experiment than in the simulations due to the differences in equations of state (§2.1.2) but this does not significantly affect the evolution of the RMI.

Simulation images at $t = 0$ show the modulations in the transmitted shock (red-brown), interface (yellow-red) and rarefaction wave (light-dark blue). The interface is inverted compared to the initial perturbation shown in figure 1(a). The experiment does not have sufficient resolution to measure such a small amplitude and the interface is noisy and nearly flat. After inversion the perturbation grows in time with good agreement between the experiment and simulations. For example, the amplitudes in the three codes at $t = 4.2 \text{ ns}$ are within 5% of each other. While the transverse width of the spike (relative to the bubble) appears somewhat larger in the experiment than in the simulations, some of this may be due to the poor instrumental resolution and the spatial averaging inherent in radiography.

Apparent in the simulation images is a criss-cross pattern in the foam (on the left). These density variations, on the order of 6%, are generated by the transmitted shock as it self-interacts. This shock, while smooth and approximately sinusoidal after refracting through the interface, eventually forms sharp kinks in regions of convergence. At these kinks complex shock interactions develop, such as Mach triple points, which

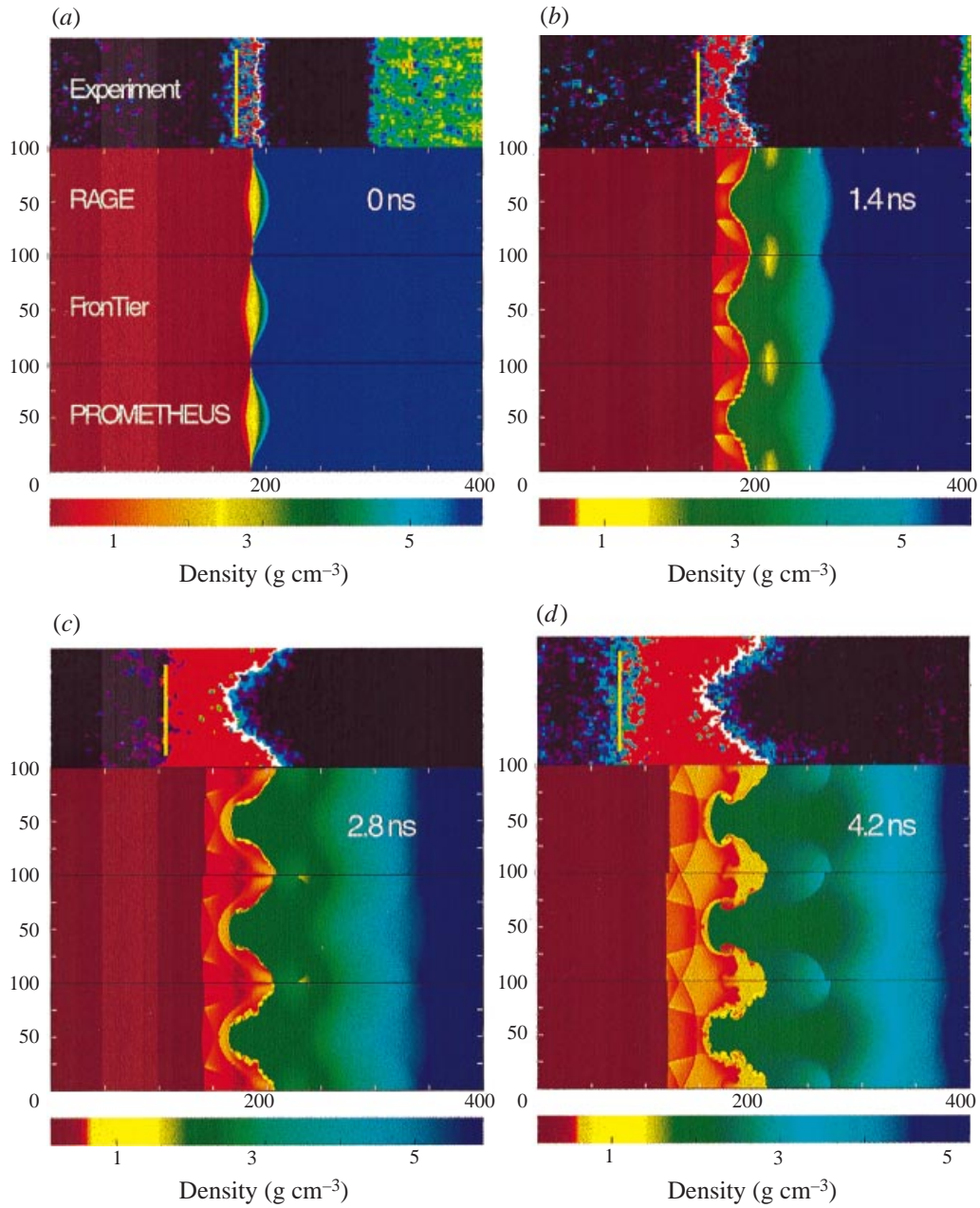


FIGURE 3. Simulation density plots and experimental radiographs for case 10/15.3. (a) $t = 0.0$ ns, (b) $t = 1.4$ ns, (c) $t = 2.8$ ns, (d) $t = 4.2$ ns. Each figure shows the results obtained with the three codes (RAGE, FronTier and PROMETHEUS, top-to-bottom) along with an experimental image. The incident shock moves from right to left. The experimental radiograph is an averaged composite over four wavelengths. Note that at later times the experimental wavelength increases due to expansion of the experimental target.

result in the formation of slip lines marking sharp changes in density and flow velocity. The points of interaction move back and forth across the domain as the transmitted shock moves, resulting in the observed pattern. The pressure plots from the simulations (not shown) also reveal the shocks generated at these interaction points (pressure jumps of about 20% at 4.8 ns) which move back toward the interface and affect the development of the spike, although the effect of these shocks on the spike is not as great as the effect of the already mentioned shocks from the rarefaction wave which strike the bubble. While the different simulation methods give results for the growth rates that are in close agreement, their predictions for the fine-scale structure of the interface profiles differ. We note, for example, that at 1.4 ns PROMETHEUS shows substantial grid-generated Kelvin–Helmholtz instability that significantly affects the shape of the interface at later times. A similar phenomenon was seen in comparisons to the code CALE in Kane *et al.* (1997). This enhanced Kelvin–Helmholtz instability is not observed for less-resolved PROMETHEUS simulations and is due, in part, to the low numerical diffusion of the PPM scheme at the interface. Kelvin–Helmholtz instability is also seen in the early-time FronTier and RAGE calculations, but is much less prominent. This is for different reasons in the two codes. In FronTier the seeds of the instability are much smaller than in the other two codes since it uses a piecewise linear curve to represent the initial conditions. In addition, the FronTier code periodically redistributes the points on the interface in order to maintain a constant distance between the interface points, and this redistribution tends to suppress any very small-wavelength instabilities. RAGE has somewhat more numerical diffusion at the interface than PROMETHEUS so that the Kelvin–Helmholtz instability is washed out before it grows to significant size. We note that experimental resolution is insufficient to distinguish between the simulations with respect to this fine structure.

The variation in perturbation growth as a function of initial amplitude is presented in figures 4 and 5. Here we show plots of amplitude and growth rate for four different initial amplitudes, $a_{0-} = 4, 10, 25$ and $50 \mu\text{m}$, with the Mach number held constant at 15.3. The graphs from case 10/15.3 are reprinted here for ease of comparison. In cases 25/15.3 and 50/15.3 only the interface is tracked in the FronTier simulations – the incident shock and scattered waves are captured by the underlying finite difference scheme. This is due to the fact that for these large initial amplitudes the shock-contact refraction is irregular and generates complicated Mach triple-point configurations that we choose not to follow.

We identify two types of nonlinear behaviour in the growth rates, early and late phase, that are differentiated by the value of the initial amplitude. With small initial amplitude, 4 and $10 \mu\text{m}$, there is good quantitative agreement with the compressible linear theory early in time as expected, but not late in time (see figures 5*a* and 5*b*). For example, the growth rate in the simulations and nonlinear theory decays by 50% near 8 ns for $a_{0-} = 4 \mu\text{m}$ and near 3 ns for $a_{0-} = 10 \mu\text{m}$. Both occur when the amplitude reaches $ka \approx 1$ ($a \approx 20 \mu\text{m}$) as observed by Aleshin *et al.* (1988), although the exact timing of the decrease is affected by the oscillations due to transverse waves. The behaviour is quite different for $a_{0-} = 25$ and $50 \mu\text{m}$ (figures 5*c* and 5*d*) in that the linear theory fails during the initial rise in the growth rate. The peak growth rates in the simulation are about half of the linear growth rates, but they are similar to $s_t - u_c \sim 15 \mu\text{m ns}^{-1}$ (arrow in figure 5*d*). This is interesting because it suggests that the nonlinearities act to keep the spike penetration into the upstream fluid behind the transmitted shock.

By distinguishing between these two manifestations of nonlinearity we can estimate

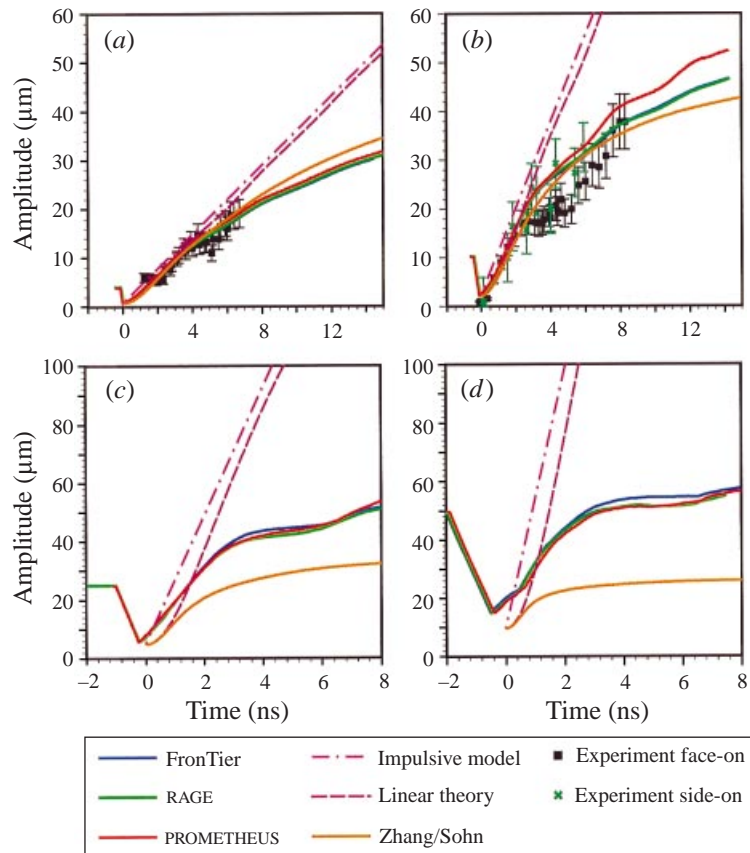


FIG. 4

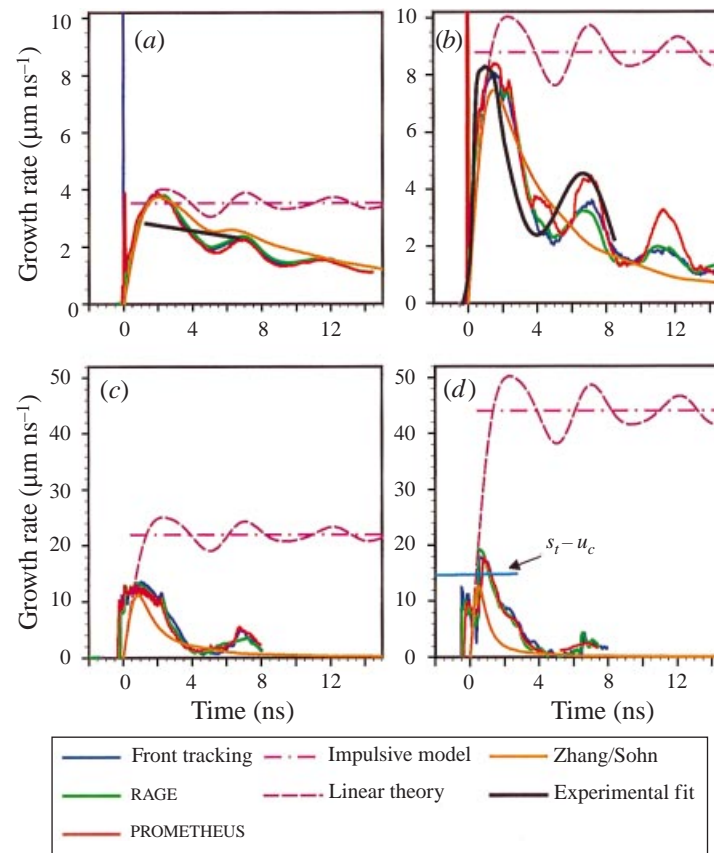


FIG. 5

FIGURE 4. Comparison of experimental, simulation and theoretical predictions for perturbation amplitude for a Mach 15.3 incident shock, (a) $a_0 = 4 \mu\text{m}$, (b) $a_0 = 10 \mu\text{m}$, (c) $a_0 = 25 \mu\text{m}$, (d) $a_0 = 50 \mu\text{m}$. The wavelength is held constant at $100 \mu\text{m}$.

FIGURE 5. As figure 4 but for growth rate. In (d) we show the difference between the transmitted shock and interface speeds (see text). This value is the same for all cases shown in this figure.

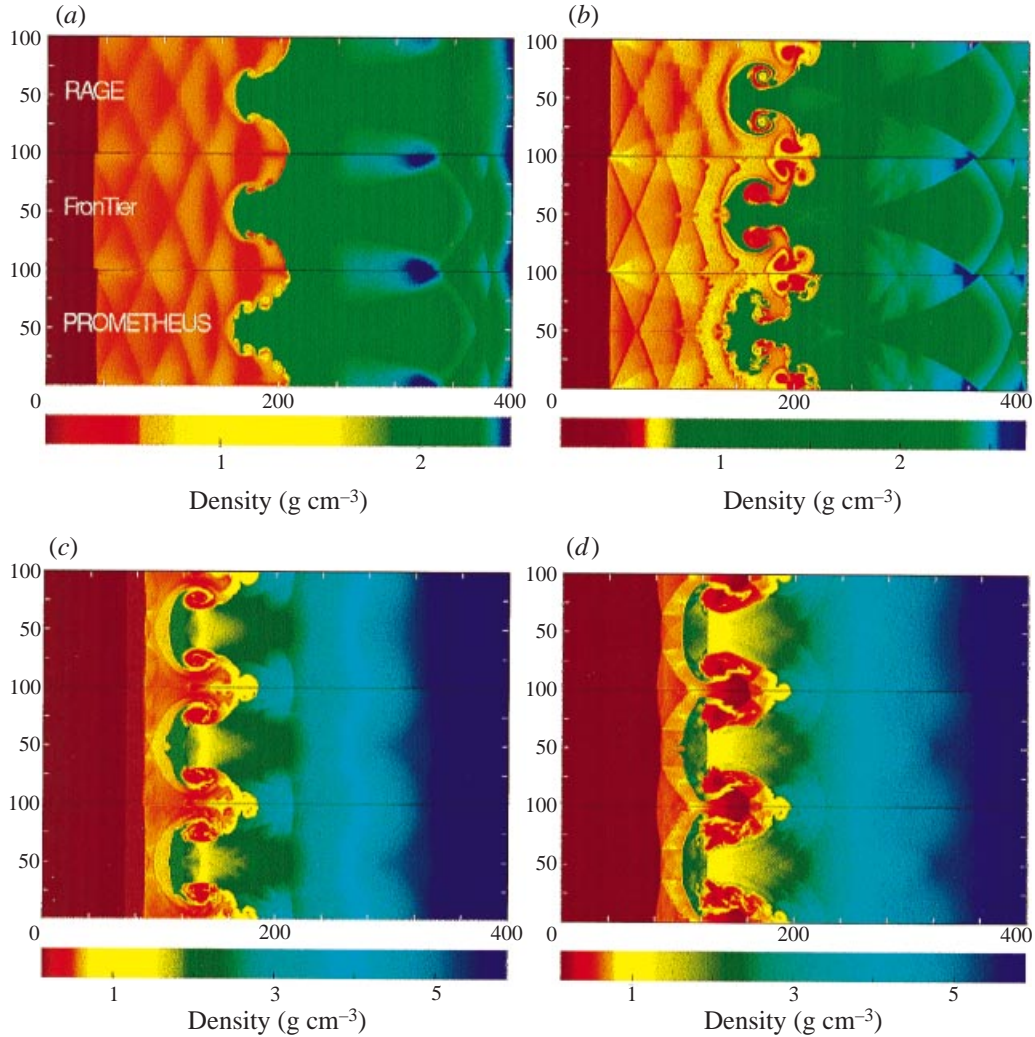


FIGURE 6. Density plots at late times. Each plot compares the interface development obtained with the three codes. (a) Case 4/15.3, $t = 9.5$ ns, (b) 10/15.3, $t = 9.6$ ns, (c) 25/15.3, $t = 3.0$ ns, (d) 50/15.3, $t = 2.5$ ns. Each figure shows the results of the three codes (RAGE, Frontier and PROMETHEUS, top-to-bottom).

the applicability of the nonlinear theory. This is possible because (2.2) is obtained by matching the asymptotic solution with the early-time linear theory. Thus, when the peak growth rate reaches the linear value the nonlinear theory is accurate as observed in figures 5(a) and 5(b). When the peak growth is suppressed strongly as in figure 5(d) the nonlinear theory underestimates the growth rate throughout. The transition occurs at $a_{0-} = 25 \mu\text{m}$ for which the nonlinear theory is able to describe the initial 50% reduction in growth rate.

In addition to suppression of the peak growth rate we observe that later growth is also greatly reduced in the large initial amplitude cases ($25 \mu\text{m}$ and $50 \mu\text{m}$). This is most clear in the case 50/15.3 which barely recovers its initial pre-shock amplitude even after 8 ns.

These nonlinear effects are evident in the simulation images shown in figure 6 at

similar amplitudes. For reference, the case with $4\ \mu\text{m}$ initial amplitude (figure 6a) has a nearly symmetric interface with weak Kelvin–Helmholtz (KH) vortices with the transmitted shock front flat and well ahead of the interface. As a_{0-} increases the features become more complex. The small KH vortices turn into long filaments. The slip lines are stronger (6% in density for 10/15.3 compared to 4% for 4/15.3) and, in the case of PROMETHEUS, exhibit KH activity. The transmitted shock remains very close to the spike causing the shock to remain modulated and the tip of the spike to flatten, especially in the 25/15.3 and 50/15.3 cases. This behaviour supports the hypothesis that the nonlinear reduction of the growth rate acts to limit the spike penetration to that of the transmitted shock. This reduction does not occur for the bubbles because the speed of the rarefaction wave is significantly larger than that of the interface. This may cause the perturbations to be more symmetric at high Atwood number as the Mach number increases since by mass conservation the normally thinner spike will have to fatten if it is not able to grow sufficiently fast.

A surprising aspect of the large-amplitude cases is the agreement among the simulations. Our growth measure, the difference in velocities and positions at the extreme points of the interface, is very sensitive to any secondary structures on the interface. As seen in figure 6, the interfaces are quite complicated, yet the agreement between predicted growth rates and amplitude is good.

We note the ‘dimple’, or tip-splitting, in the spike, that is most noticeable in figure 6(b). As these features have been observed in other experiments (Aleshin *et al.* 1996) we believe that the splitting is physical, although resolution in the current experiments is insufficient to resolve such structure. The RAGE images do not show the splitting, but the figures do indicate flattening. This is likely due to under-resolution near the interface – the grids chosen are sufficient for convergence in growth rate, but consideration was not given to resolving such secondary features (see the Appendix).

The effect of nonlinearities can be quantified by plotting the peak growth rate vs. ka_{0-} as shown in figure 7. Although it can be short lived, the peak growth rate is useful because it is the most reliable measurement: peak growth occurs early in time when the experimental radiographs are crisper and the target decompression is minimal. In addition, it is the best measure of the nonlinearity due to the initial conditions.

The growth rate in figure 7 is scaled to the Meyer–Blewett version of the Impulsive Model (Meyer & Blewett 1972), $\dot{a}_{IM} = A^* u_c k a_{0\pm}$, because it describes the linear peak growth very well. The agreement among the measurements and calculations in figure 7 is good. The peak growth rates are within 20% of that obtained from the Impulsive Model for $ka_{0-} < 1$, but decrease significantly for larger ka_{0-} . The breakdown of the linear theory with ka_{0-} is expected, but the failure mechanism is unclear.

We gain some insight into how the linear theory fails and how nonlinearities affect the dynamics at high Mach numbers by comparing the linear growth rates with the shock speeds, an approach discussed earlier. For example, at $ka_{0-} = 3$ we obtain $\dot{a}_{IM} \approx 45\ \mu\text{m ns}^{-1}$, which is three times the difference between the speeds of the transmitted shock and the interface, namely, $s_t - u_c = 14.9\ \mu\text{m ns}^{-1}$. Thus, if linear theory were to apply for very long, the spike tip would overtake the transmitted shock. Since such spike penetration is energetically prohibitive we propose a nonlinear correction factor

$$F_{nl} = \frac{1}{1 + \dot{a}_{IM}/(s_t - u_c)}.$$

This expression is empirically derived and constructed so that the predicted nonlinear growth rate, $\dot{a}_{IM} \times F_{nl}$, is always less than the difference between the interface and

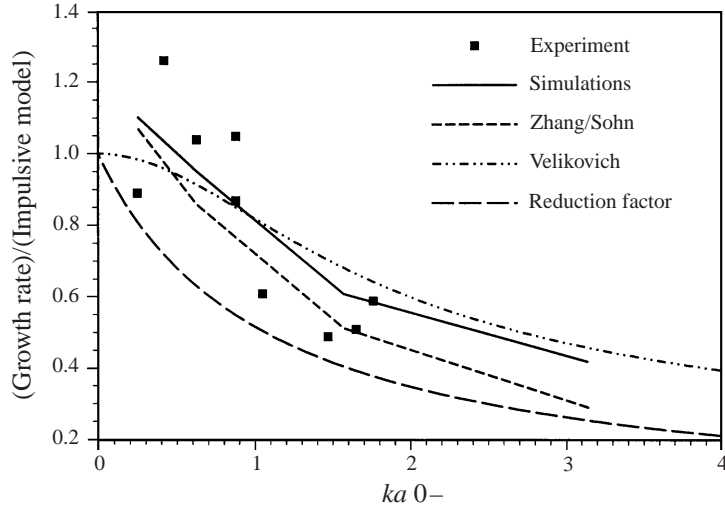


FIGURE 7. Comparison of experimental, simulation and theoretical peak growth rates as a function of initial amplitude with incident Mach number 15.3. Growth rates are scaled to the Meyer–Blewett formulation of the Impulsive Model. For the simulations we averaged the peak growth rates of each of the three codes.

transmitted shock speeds and tends to the impulsive growth rate, \hat{a}_{IM} , in the linear regime. It is in fairly good agreement with the results in figure 7 as indicated by the dashed line. For fixed initial amplitude the correction is important mainly for strong shocks since s_t/u_c decreases with increasing Mach number of the transmitted shock while the induced growth rate would be expected to increase. For our materials, $F_{nl} \sim 0.5$ at $ka_{0-} = 1$ for Mach 15.3 shocks where $s_t \sim 1.25u_c$. For Mach 1.33, $F_{nl} \sim 0.9$ where $s_t \sim 6u_c$.

3.2. Incident shock strength variations

In this section we explore the effects of compression by varying the incident shock strength, keeping the initial amplitude fixed at $4\mu\text{m}$.

Figures 8 and 9 show results from calculations and theories for incident shock Mach numbers of 1.33, 5.6, 10.8 and 15.3 and experimental data for the latter two. Please note that the time and amplitude scales differ between plots because the growth rate increases with Mach number.

For Mach 1.33, the compression is weak and the phase reversal is indirect, i.e. it occurs after the shock refraction is complete (Yang *et al.* 1994). With the values given in table 2 in the Appendix, the magnitude is consistent with figure 8(a) at $t = 0$. Since the Atwood number is negative the growth rate is negative at approximately $-0.2\mu\text{m ns}^{-1}$ and the amplitude crosses zero near $t = a_{0+}/(da/dt) \approx 10\text{ ns}$. Thus, the magnitude of $a(t)$ decreases in figure 8(a) until about 10 ns and then increases following the phase inversion. For Mach 5.6 the phase inversion occurs during the shock traversal of the interface because $s_i = 18.2\mu\text{m ns}^{-1} < u_c = 21\mu\text{m ns}^{-1}$. Thus, $a_{0+} = a_{0-}(1 - u_c/s_i) = -0.66\mu\text{m}$ and the phase inversion is direct. The results are similar at Mach 10.8 and 15.3 since $s_i < u_c$. The transition between direct and indirect inversion occurs at approximately Mach 3 for these materials. Both types of inversion have been observed at Mach 15 using different materials (Dimonte *et al.* 1996).

The NOVA experiments at Mach 10.8 and 15.3 obtain amplitudes and growth rates which are slightly smaller than those in the calculations (Figures 8c, d and 9c, d), but

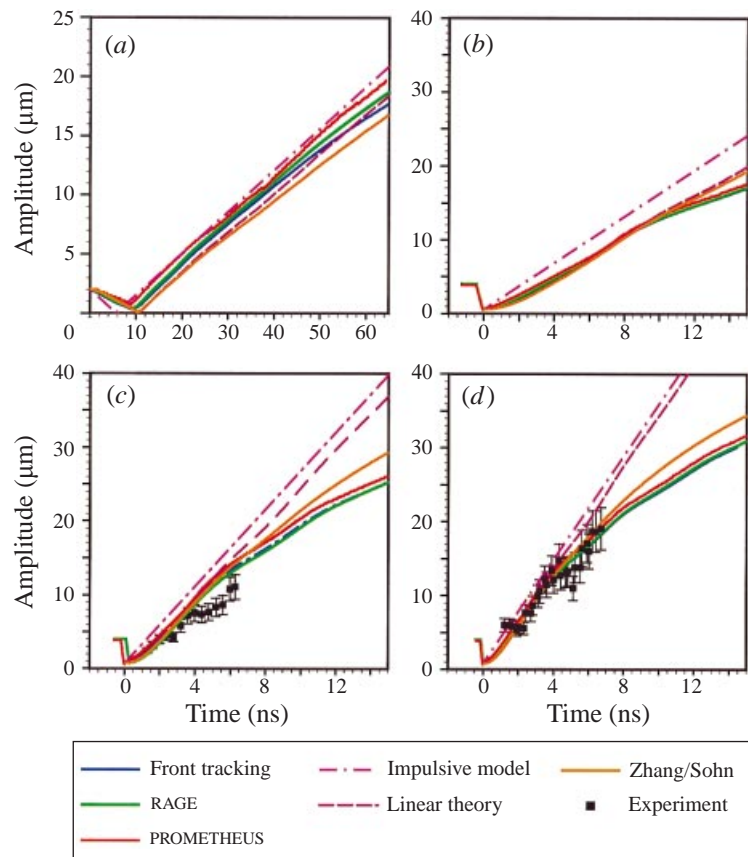


FIG. 8

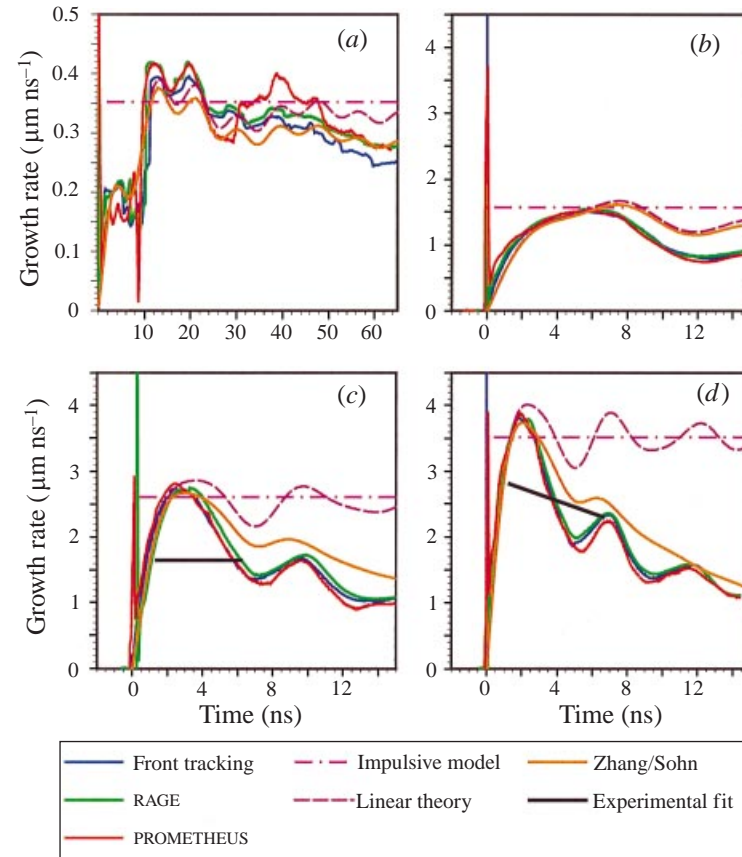


FIG. 9

FIGURE 8. Comparison of simulation and theoretical predictions for perturbation amplitudes for initial amplitude of $4 \mu\text{m}$. (a) Mach 1.33 incident shock, (b) Mach 5.6, (c) Mach 10.8, (d) Mach 15.3.

FIGURE 9. As figure 8 but for perturbation growth rates.

they are within the experimental error indicated. We also note that the agreement among the simulations is very good for Mach numbers of 5.6 and above, but the agreement is poorer at Mach 1.33. At 40 ns in case 4/1.33 there is a 20% difference between the growth rates predicted by FronTier and by PROMETHEUS, although at earlier times the agreement is better. We believe that this is due to two factors. One is that the post-shock perturbation amplitude is smaller than in the other cases and, in fact, continues to decrease for some period after shocking. This means that the perturbation is not as well resolved, leading to larger numerical errors and difficulties in determining the interface position for calculation of the amplitude and growth rate. The second factor is the indirect inversion phenomenon. Interface plots of indirect inversion show a complicated ‘double hump’ shape after shock refraction rather than the more sinusoidal shape seen in the cases where direct inversion occurs. It appears that the interface is quite sensitive to the details of the numerical scheme when it is in this potentially unstable regime.

Linear theory is able to obtain the peak growth rates quite well in these cases since $ka_{0-} < 1$, but it fails sooner as the shock strength is increased. For example, for Mach 1.33 the growth rate peaks near 10 ns and decreases by only 20% over the entire 65 ns. For Mach 15.3, the growth rate peaks near 2 ns but it decreases by a factor of three by 14 ns. By comparing the different speeds s_i , u_c and s_t at the various Mach numbers, we find that the time to peak growth is related to the distance travelled by the transmitted shock, namely, $\sim 15 \lambda/s_t$. The decay of the growth rate after the peak may be related to the large amplitude ($ka_{0+} \sim 1$). For Mach numbers larger than 5.6, we find that the growth rate is approximately half of the linear rate when $a(t) \sim 15\text{--}20 \mu\text{m}$ ($ka \sim 1$). This does not seem to apply at Mach 1.33 since the growth rate is reduced by only 20% at $t = 65$ ns even though the amplitude has reached $17 \mu\text{m}$ ($ka(t) = 1.1$).

The nonlinear theory is able to describe the decay of the growth rate as the amplitude increases for all Mach numbers except Mach 5.6. In this case it follows the linear growth rate rather than those of the simulations.

One of the most important factors associated with strong shocks is the reduction in growth rate due to compressibility. The effect of compression is highlighted in figure 10 by plotting the peak growth rate vs. Mach number. We include here the predictions of the nonlinear model of Velikovich (Velikovich & Dimonte 1996). We chose cases with $ka_{0-} < 1$ to minimize nonlinear effects with the growth rate scaled to the uncompressed linear growth rate ($Aku_c a_{0-}$) to remove the obvious dependencies on speed and density. Except for the Richtmyer formulation of the Impulsive Model, simulations and analytical theories are in good agreement and show a steady decrease in the scaled growth rate from 1.0 at small Mach number to 0.25 at Mach 15.3. Most of the peak growth rate reduction occurs for Mach numbers less than 5 and it is relatively insensitive to increases in the Mach number above this value. The source of this reduction can be seen with the aid of the impulsive models. For $A < 0$, the Meyer–Blewett formulation of the Impulsive Model is appropriate and this ratio is $(A^*/A)/[\frac{1}{2}(1 + (1 - u_c/s_i))]$. This relation suggests two sources for the reduction in growth rate. First, the factor A^*/A is due to the material compression and this occurs even for flat interfaces (Riemann problem). The second factor is due to the geometric compression of the perturbations at the interface by the shock and represents the average of the pre- and post-shock amplitudes. As was pointed out by (Meyer & Blewett (1972)), Richtmyer’s version of the Impulsive Model using the post-shock amplitude $a_{0-}(1 - u_c/s_i)$ fails for $A < 0$, and this is indicated in figure 10. In fact, the Richtmyer formula changes sign near Mach 3 because there is a direct phase

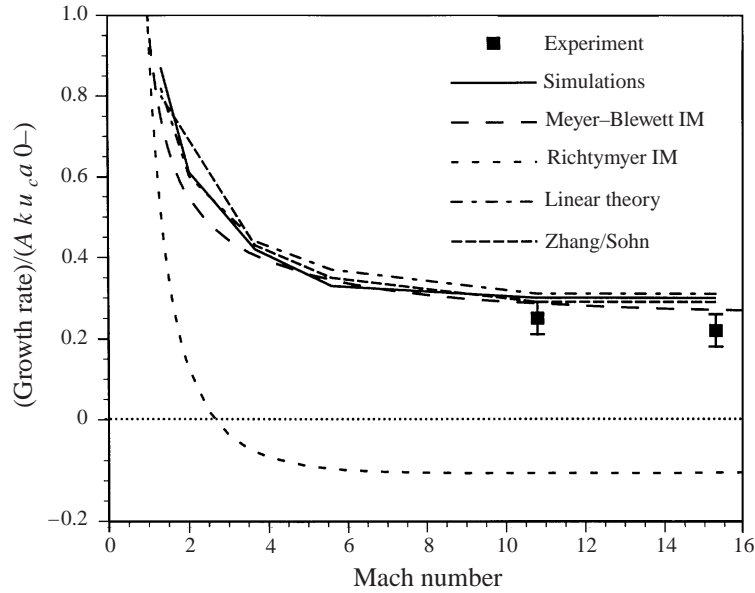


FIGURE 10. Comparison of experimental, simulation and theoretical peak growth rates as a function of incident shock Mach number. The growth rate is scaled by $Aku_c a_0^-$.

inversion for Mach numbers above this point. This critical Mach number depends on the material densities and gammas, but it can be estimated by solving the Riemann problem. It would be very instructive to perform experiments with Mach numbers in the range of 1 to 4 to fill the gap between the incompressible and NOVA regimes.

4. Conclusion

We have used a variety of methods – experiment, simulation and theory – to investigate Richtmyer–Meshkov instability in order to evaluate the methods and to study the effects of compression and nonlinearity on instability growth. This is done by varying the initial amplitude of the interfacial perturbations and the Mach number of the incident shock while keeping the materials and the perturbation wavelength constant.

We compare the results of experiments, numerical simulations, linear theory and nonlinear theories. Although impulsive models are approximate, we also evaluate them because they provide insight and simple estimates of the growth rate.

There is remarkable agreement among the various methods evaluated in this investigations in the respective regions of validity, despite the high Mach number and compression. Linear theory is able to describe the initial evolution of the instability obtained from the simulations and experiment as long as $ka_0^- < 1$. The peak growth rates agree with the estimate of the Meyer–Blewett model, but not with the Richtmyer model. The time-dependent nonlinear theory does a good job of describing the initial rise of the growth rate to the linear value and its subsequent average decay as the amplitude exceeds $1/k$. Since it is matched to the linear theory initially, it underestimates the growth rate observed in the simulations when $ka_0^- > 1$. Also, the oscillations in the growth rate are diminished because it does not include the shock reverberations in the upstream fluid. The nonlinear model of Velikovich is able to

describe the early-time reduction in the peak growth rate when $ka_0 > 1$, but not the late-time decay because it is not time dependent.

The three simulations with different numerical techniques agree on the large-scale structure, such as the amplitude of the interface perturbation. They are able to describe the experimental results even though they approximate the equation of state by perfect gases. The simulations exhibit differences in the small-scale structure, such as the Kelvin–Helmholtz roll-up at the interface and slip lines in the upstream fluid which may be important in the molecular mixing of the two fluids. The experiments are able to measure the large-scale structure without the liability of membranes and edge effects. However, they are not able to measure the small-scale structure that distinguishes the numerical simulations. Thus, future experiments need to have good resolution, but our results suggest that strong shock effects can be studied at Mach numbers as low as five.

The effect of compression was studied with $ka_{0-} < 1$ by varying the Mach number of the incident shock. This changes not only the fluid densities, but also the relations between the various wave speeds. Near Mach 1, the compression is minimal and all models agree with the simulations, namely the growth rate da/dt is $Au_c ka_{0-}$ and there is an indirect phase inversion since $u_c < s_i$ and $da/dt < 0$. At Mach 15.3, the shock is essentially of infinite strength and the compression effects are evident. The first fluid is compressed nearly four-fold by the incident shock, but the decompression wave is large due to the density mismatch and this leaves its final density only 30% larger. The second fluid is compressed five-fold which makes the post-shock Atwood number $A^* = -0.6$. The interface undergoes a direct phase inversion in this case, namely $a_{0+} \approx -0.2a_{0-}$ because the incident shock speed is smaller than the shocked contact speed, i.e. $u_c > s_i$, for such a strong shock. This compression is described well by linear theory, numerical simulations and experiments. They all obtain a peak growth rate consistent with the Meyer–Blewett impulsive model, $A^*u_c ka_{0\pm} \sim -9 \mu\text{m ns}^{-1}$ and which is much smaller than the uncompressed estimate $Au_c ka_{0-} \sim -35 \mu\text{m ns}^{-1}$. The Richtmyer model gives $A^*u_c ka_{0+} \approx 5 \mu\text{m ns}^{-1}$ and has both the wrong magnitude and sign. As indicated earlier in figure 10, the growth rate decreases relative to $Au_c ka_{0-}$ between Mach 1 and Mach 5 due to the compression effects. The growth rate then remains at about $0.2Aku_c a_0$ for Mach numbers greater than five since this represents the infinite shock limit.

Nonlinearities are very important and occur at different times depending on ka_{0-} . For $ka_{0-} \ll 1$, the growth rate is initially given by the linear theory, but it decays later in time as the amplitude grows to $ka \sim 1$. This is described nicely by experiments, simulations and the nonlinear theory. For $ka_{0-} > 1$, the behaviour is nonlinear immediately and the growth rate never attains the value given by linear theory. In fact, the peak growth rate scaled to the linear value decreases steadily with ka_{0-} . This investigation is conducted with a Mach 15.3 shock in which the velocities of the transmitted shock and interface are comparable, $s_t/u_c \sim 1.25$. This is an interesting regime because the linear growth rate is larger than $s_t - u_c$ for $ka_{0-} > 1$. In this case, the nonlinear reduction in growth rate keeps the spike penetration into the downstream fluid behind the transmitted shock. This effect may not be as important at low Mach numbers where $s_t \gg u_c$. Thus, we might expect the spikes and bubbles to become more symmetric at high Atwood number as the Mach number increases.

For inertial confinement fusion applications, Richtmyer–Meshkov instability occurs in a more complicated setting. For example, the interface between the fluids is perturbed in a random fashion and the problem has a spherical geometry rather than rectangular geometry. It is our hope that the comparison study presented here will

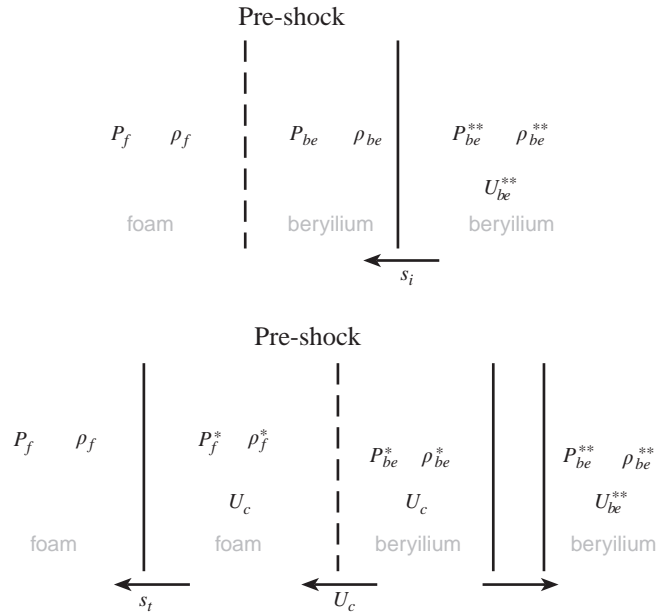


FIGURE 11. Guide to symbols. P , ρ , u and s refer to pressure, density, flow speed and shock speed, respectively.

provide useful guidance for further studies of the Richtmyer–Meshkov instability in these more complicated settings.

Appendix. Initialization of simulations and models

The material and flow parameters used in the simulations are given in table 2 with symbols defined schematically in figure 11. The geometry is the same as in figure 1 and all positive velocities are oriented to the left. The velocities listed in the table have been adjusted so that the post-shock contact is approximately stationary. If the problems are to be run in the laboratory frame, u_c (listed in the table) should be added to each velocity and the suggested domains changed accordingly.

All computations were performed with a domain width of one full wavelength, although symmetry in the x -direction could be used to cut this width in half. Table 3 lists domain lengths and initial interface placements used in the simulations. The domain lengths are optimized by observing that if flow-through boundary conditions are used at the right and the left of the domain, the computations are unaffected by boundary signals until the time that reflected signals from exiting transmitted and reflected waves reach the contact. The one-dimensional unperturbed problem is solved to determine wave placements that maximize the time for these signals to arrive at the contact. The length of the domain is set such that this maximum time is at least as long as the time of the simulation. Note that these domain sizes and interface placements are appropriate only if the incident shock is initialized near the interface. Because the domain constraints for the Mach 15.3 case are the most stringent, the domains for all cases used those dimensions. The domains for the large-amplitude cases were enlarged somewhat to account for the larger time of refraction, although the shorter time of simulation probably made this unnecessary. We see no evidence of boundary signals in our data.

	Simulation number						
	10/15.3	4/15.3	4/10.8	4/5.6	4/1.33	25/15.3	50/15.3
a_{0-}	10	4	4	4	4	25	50
λ				100			
Mach num.	15.3	15.3	10.8	5.6	1.33	15.3	15.3
ρ_f				0.12			
P_f				0.1			
c_f				10.99			
u_f	-59.44	-59.44	-41.70	-20.95	-2.169	-59.44	-59.44
ρ_{Be}				1.7			
P_{Be}				0.1			
c_{Be}				3.254			
u_{Be}	-59.44	-59.44	-41.70	-20.95	-2.169	-59.44	-59.44
ρ_{Be}^{**}	5.887	5.887	5.825	5.511	2.466	5.887	5.887
P_{Be}^{**}	30.07	30.07	14.97	4.003	0.1989	30.07	30.07
c_{Be}^{**}	30.32	30.32	21.51	11.43	3.810	30.32	30.32
u_{Be}^{**}	-24.03	-24.03	-16.81	-8.35	-0.825	-24.03	-24.03
ρ_f^*	0.5956	0.5956	0.5496	0.4063	0.1454	0.5956	0.5956
P_f^*	5.410	5.410	2.770	0.8470	0.1323	5.410	5.410
c_f^*	36.29	36.29	27.03	17.37	11.49	36.29	36.29
u_f^*				0			
ρ_{Be}^*	2.270	2.270	2.281	2.325	1.965	2.270	2.270
P_{Be}^*	5.410	5.410	2.770	0.8470	0.1323	5.410	5.410
c_{Be}^*	20.71	20.71	14.78	8.098	3.481	20.71	20.71
u_{Be}^*	0						
u_c	59.44	59.44	41.70	20.95	2.169	59.44	59.44
s_i	49.79	49.79	35.14	18.22	4.328	49.79	49.79
s_t	74.44	74.44	53.35	29.73	12.40	74.44	74.44
γ_f				1.45			
γ_{Be}				1.8			

TABLE 2. Material and flow parameters for simulations and models. The geometry is as in figure 1 and the symbols are defined in figure 11 with the state variables obtained from one-dimensional solutions. The subscripts f and Be refer to foam and beryllium, respectively. Velocities are given in $\mu\text{m ns}^{-1}$ (10^5 cm s^{-1}), lengths in μm (10^{-4} cm), densities in g cm^{-3} and pressures in megabars ($10^{12} \text{ g cm}^{-1} \text{ s}^{-2}$). u_c is the velocity of an unperturbed contact after shocking, s_i is the speed of the incident shock and s_t is the speed of the transmitted shock, all measured in the laboratory frame with positive speeds to the left. All velocities other than u_c , s_i and s_t have been translated by u_c so that the shocked interface is approximately stationary during the computation. The interface is initialized as $z(x) = a_{0-} \cos(2\pi x/100)$.

	Initial amplitude	
	4 or 10 μm	25 or 50 μm
Domain width	100 μm	100 μm
Domain length	400 μm	500 μm
Interface position	200 μm	150 μm

TABLE 3. Domain size and interface position for simulations. The values for the simulations with initial amplitude of 4 and 10 μm are given in the first column while the values for simulations with initial amplitudes of 25 and 50 μm are given in the second. These values assume that the incident shock is near refraction at initialization and that the computations are done in a frame with an approximately stationary shock, i.e. with the velocity parameters given in table 2.

Each code initialized the incident shock differently. RAGE initialized the incident shock through an overlay from a one-dimensional computation where the one-dimensional problem was run sufficiently long for the shock to reach its steady-state profile. The PROMETHEUS runs achieved a steady shock very quickly and were initialized with the shock far enough from the interface to enable it to do so. Since FronTier has steady-state shocks at initialization when a tracked incident shock is used, no overlay procedure was needed in those cases. In the two cases where an untracked shock was used, 25/15.3 and 50/15.3, the incident shock was initialized far from the interface (at least 50 zones distant). The interface was positioned such that its position at the time of refraction was approximately that given in table 3. Since the interface is tracked in all cases diffusion of the interface does not occur in the relatively long period leading to refraction.

The computational grids used in our simulations were sufficient to ensure that the late-time amplitudes (last time plotted) varied by less than 5% from a grid with one-half the refinement. In most cases a much smaller difference was seen. All PROMETHEUS runs used uniform grids of 480 zones across one wavelength ($\Delta x = 0.208 \mu\text{m}$) while RAGE used adaptive grids with smallest zones of dimension $\Delta x = 0.156 \mu\text{m}$ corresponding to 640 zones across one wavelength. The FronTier simulations of cases 25/15.3 and 50/15.3 used uniform grids of 200 zones across ($\Delta x = 0.5 \mu\text{m}$) while the others used grids of 300 zones ($\Delta x = 0.33 \mu\text{m}$). Note that the FronTier simulations with initial amplitudes of 25 and 50 μm did not use a tracked incident shock.

R.L.H., G.D., M.L.G., J.W.G., M.S., D.H.S. and R.P.W. were supported by the US Department of Energy. R.L.H. was also supported by a National Science Foundation Mathematical Sciences Postdoctoral Fellowship, while J.W.G. received additional support from grants NSF DMS-9500568 and ARO DAA H04-95-10414. B.F. was supported by NASA Earth and Space Science High Performance Computing and Communications Program grant NAG5-2652. A.L.V. was supported by the US Department of Energy through contract with the Naval Research Laboratory and Q.Z. was supported in part by the US Department of Energy, contract DE-FG02-90ER25084, by subcontract from Oak Ridge National Laboratory (subcontract 38XSK964C) and by National Science Foundation contract NSF-DMS-9500568.

This work was performed under the auspices of the US Department of Energy by LLNL under contract number W-7405-ENG-48 and by LANL under contract number W-7405-ENG-36.

REFERENCES

- ALESHIN, A. N., CHEBOTAREVA, E. I., KRIVETS, V. V., LAZAREVA, E. V., SERGEEV, S. V., TITOV, S. N. & ZAYTSEV, S. G. 1996 Investigation of evolution of interface after its interaction shock waves. *Tech. Rep.* 02-96 and 06-96. International Institute for Applied Physics and High Technology, Moscow, Russia.
- ALESHIN, A. N., GAMALLI, E. G., ZAITSEV, S. G., LAZAREVA, E. V., LEBO, I. G. & ROZANOV, V. B. 1988 Nonlinear and transitional stages in the onset of the Richtmyer–Meshkov instability. *Sov. Tech. Phys. Lett.* **14**, 466–468.
- ALON, U., HECHT, J., MUKAMEL, D. & SHVARTS, D. 1994 Scale invariant mixing rates of hydrodynamically unstable interfaces. *Phys. Rev. Lett.* **72**, 2867–2870.
- ALON, U., HECHT, J., OFER, D. & SHVARTS, D. 1995 Power laws and similarity of Rayleigh–Taylor and Richtmyer–Meshkov mixing fronts at all density ratios. *Phys. Rev. Lett.* **74**, 534–538.
- BALTRUSAITIS, R. M., GITTINGS, M. L., WEAVER, R. P., BENJAMIN, R. F. & BUDZINSKI, J. M. 1996 Simulation of shock-generated instabilities. *Phys. Fluids* **8**, 2471–2483.
- BENJAMIN, R. 1992 Experimental observations of shock stability and shock induced turbulence. In *Advances in Compressible Turbulent Mixing* (ed. W. P. Dannevik, A. C. Buckingham & C. E. Leith), pp. 341–348. 5285 Port Royal Rd. Springfield VA 22161: National Technical Information Service, U.S. Department of Commerce.
- BENJAMIN, R., BESNARD, D. & HAAS, J. 1993 Shock and reshock of an unstable interface. LANL Rep. LA-UR 92-1185, NTIS #DE91014737. Los Alamos National Laboratory.
- BESNARD, D., GLIMM, J., HAAS, J. F., RAUENZAHN, R. M., RUPERT, V. & YOUNGS, D. 1991 Numerical simulation of 2D shock-tube multimaterial flow. In *Proc. Third Intl Workshop on The Physics of Compressible Turbulent Mixing at Royaumont France*.
- BURROWS, A., HAYES, J. & FRYXELL, B. 1995 On the nature of core-collapse supernova explosion. *Astrophys. J.* **450**, 830.
- CHERN, I.-L., GLIMM, J., MCBRYAN, O., PLOHR, B. & YANIV, S. 1986 Front tracking for gas dynamics. *J. Comput. Phys.* **62**, 83–110.
- CLOUTMAN, L. D. & WEHNER, M. F. 1992 Numerical simulation of Richtmyer–Meshkov instabilities. *Phys. Fluids A* **4**, 1821–1830.
- COLELLA, P. 1985 A direct Eulerian MUSCL scheme for gas dynamics. *SIAM J. Comput.* **6**, 104.
- COLELLA, P. & WOODWARD, P. 1984 The piecewise parabolic method (PPM) for gas-dynamical simulation. *J. Comput. Phys.* **54**, 174.
- DIMONTE, G., FRERKING, C. E., SCHNEIDER, M. & REMINGTON, B. 1996 Richtmyer–Meshkov instability with strong radiatively driven shocks. *Phys. Plasmas* **3**, 614–630.
- DIMONTE, G. & REMINGTON, B. 1993 Richtmyer–Meshkov experiments on the nova laser at high compression. *Phys. Rev. Lett.* **70**, 1806–1809.
- EMERY, M. H., GARDNER, J. H., LEMBERG, R. H. & OBENSCHAIN, S. P. 1991 Hydrodynamic target response to an induced spatial incoherence-smoothed laser beam. *Phys. Fluids B* **3**, 2640–2651.
- FRYXELL, B., MÜLLER, E. & ARNETT, D. 1989 Hydrodynamics and nuclear burning. *Rep. No.* 449. Max-Planck-Institut für Astrophysik.
- FRYXELL, B. & TAAM, R. 1988 Numerical simulations of non-axisymmetric accretion flow. *Astrophys. J.* **335**, 862.
- GITTINGS, M. L. 1992 SAIC's adaptive grid Eulerian hydrocode. In *Defense Nuclear Agency Numerical Methods Symposium, 28-30 April 1992*.
- GLIMM, J., LI, X. L., MENIKOFF, R., SHARP, D. H. & ZHANG, Q. 1990 A numerical study of bubble interactions in Rayleigh–Taylor instability for compressible fluids. *Phys. Fluids A* **2**, 2046–2054.
- GLIMM, J., LINDQUIST, W. B. & ZHANG, Q. 1991 *Front Tracking, Oil Reservoirs, Engineering Problems and Mass Conservation, IMA Volumes in Mathematics and its Applications*, vol. 29. Springer.
- GROVE, J. 1987 Front tracking and shock–contact interactions. In *Advances in Computer Methods for Partial Differential Equations* (ed. R. Vichnevetsky & R. Stepleman), vol. VI. New Brunswick: IMACS, Dept. of Comp. Sci., Rutgers University.
- GROVE, J., HOLMES, R., SHARP, D. H., YANG, Y. & ZHANG, Q. 1993 Quantitative theory of Richtmyer–Meshkov instability. *Phys. Rev. Lett.* **71**, 3473–3476.
- HECHT, J., ALON, U. & SHVARTS, D. 1994 Potential flow models of Rayleigh–Taylor and Richtmyer–Meshkov bubble fronts. *Phys. Fluids* **6**, 4019–4030.
- HOLMES, R. L., GROVE, J. W. & SHARP, D. H. 1995 Numerical investigation of Richtmyer–Meshkov instability using front tracking. *J. Fluid Mech.* **301**, 51–64.

- ISHIZAKI, R. & NISHIHARA, K. 1997 Propagation of a rippled shock wave drive by nonuniform laser ablation. *Phys. Rev. Lett.* **78**, 1920–1923.
- KANE, J., ARNETT, D., REMINGTON, B. A., GLENDINNING, S. G., CASTOR, J., WALLACE, R., RUBENCHIK, A. & FRYXELL, B. A. 1997 Supernova-relevant hydrodynamic instability experiments on the nova laser. *Astrophys. J.* **478**, L75–L78.
- LINDL, D. L., MCCRORY, R. L. & CAMPBELL, E. M. 1992 Progress toward ignition and burn propagation in inertial confinement fusion. *Physics Today* **45** (9), 32–40.
- MESHKOV, E. E. 1969 Instability of the interface of two gases accelerated by a shock wave. *Fluid Dyn.* **43** (5), 101–104.
- MESHKOV, E. E. 1970 Instability of a shock wave accelerated interface between two gases. *NASA Tech. Trans.* **F-13**, 074.
- MEYER, K. A. & BLEWETT, P. J. 1972 Numerical investigation of the stability of a shock-accelerated interface between two fluids. *Phys. Fluids* **15**, 753–759.
- MIKAEILIAN, K. 1996 Analytic approach to nonlinear Rayleigh–Taylor and Richtmyer–Meshkov instabilities. *Rep. UCRL-JC-125113*. Lawrence Livermore National Laboratory.
- MULLER, E., FRYXELL, B. & ARNETT, D. 1991 Instability and clumping in SN 1987a. *Astron. Astrophys.* **251**, 505–514.
- NOH, W. 1983 Artificial viscosity (q) and artificial heat flux (h) errors for spherically divergent shocks. *Rep. UCRL-89623*. Lawrence Livermore National Laboratory, Livermore, CA.
- RICHTMYER, R. D. 1960 Taylor instability in shock acceleration of compressible fluids. *Commun. Pure Appl. Maths* **13**, 297–319.
- SAMTANEY, R. & ZABUSKY, N. J. 1994 Circulation deposition on shock-accelerated planar and curved density-stratified interfaces: models and scaling laws. *J. Fluid Mech.* **269**, 45–78.
- TAYLOR, R. J., VELIKOVICH, A. L., DAHLBURG, J. P. & GARDNER, J. H. 1997 Saturation of laser imprint on ablatively driven plastic targets. *Phys. Rev. Lett.* **79**, 1861–1864.
- VELIKOVICH, A. L. 1996 Analytic theory of Richtmyer–Meshkov instability for the case of reflected rarefaction wave. *Phys. Fluids* **8**, 1666–1679.
- VELIKOVICH, A. L. & DIMONTE, G. 1996 Nonlinear perturbation theory of the incompressible Richtmyer–Meshkov instability. *Phys. Rev. Lett.* **76**, 3112–3115.
- VETTER, M. & STURTEVANT, B. 1995 Experiments on the Richtmyer–Meshkov instability of an air/SF₆ interface. *Shock Waves* **4**, 247–252.
- WOODWARD, P. & COLELLA, P. 1984 Numerical simulation of two-dimensional fluid flows with strong shocks. *J. Comput. Phys.* **54**, 115.
- WOCHUK, J. G. & NISHIHARA, K. 1996 Linear perturbation growth at a shocked interface. *Phys. Plasmas* **3**, 3761–3776.
- WOCHUK, J. G. & NISHIHARA, K. 1997 Asymptotic growth in the linear Richtmyer–Meshkov instability. *Phys. Plasmas* **4**, 1028–1038.
- YANG, Y., ZHANG, Q. & SHARP, D. H. 1994 Small amplitude theory of Richtmyer–Meshkov instability. *Phys. Fluids* **6**, 1856–1873.
- ZHANG, Q. 1996 The exact analytical solution of layzer model. *Rep. SUNY-AMS-96-26*. State University of New York at Stony Brook.
- ZHANG, Q. & SOHN, S.-I. 1996 An analytical nonlinear theory of Richtmyer–Meshkov instability. *Phys. Lett. A* **212**, 149.
- ZHANG, Q. & SOHN, S.-I. 1997a Nonlinear theory of unstable fluid mixing driven by shock waves. *Phys. Fluids* **9**, 1106–1124.
- ZHANG, Q. & SOHN, S.-I. 1997b Padé approximation to an interfacial fluid mixing problem. *Appl. Maths Lett.* **10**, 121–127.
- ZIMMERMAN, G. B. & KRUEER, W. L. 1975 *Comments Plasma Phys. Controlled Fusion* **2** (51).